

Luminosity distance and extinction by submicrometer-sized grains

R. SIEBENMORGEN,¹ FRANK HEYMANN,² AND R. CHINI^{3,4,5}

¹*European Southern Observatory,
Karl-Schwarzschild-Str. 2, 85748 Garching, Germany*

²*German Aerospace Center
Institute for solar terrestrial physics
Kalkhorstweg 53, 17235, Neustrelitz, Germany*

³*Nicolaus Copernicus Astronomical Center of the Polish Academy of Sciences,
Bartycka 18, 00-716 Warsaw, Poland;*

⁴*Ruhr University Bochum, Faculty of Physics and Astronomy,
Astronomical Institute (AIRUB),
44780 Bochum, Germany;*

⁵*Universidad Catolica del Norte, Instituto de Astronomia,
Avenida Angamos 0610, Antofagasta, Chile*

ABSTRACT

The distance to the stars is a fundamental parameter, which is determined via two primary methods – parallax and luminosity. While the parallax is a direct trigonometric method, the luminosity distance is usually influenced by interstellar extinction. As long as the optical properties of dust grains are wavelength-dependent this contamination can be corrected. However, as the grain size increases, the extinction properties become gray, meaning these particles contribute by a constant at wavelengths $\lesssim 1\mu\text{m}$, making them undetectable by photometry in the optical. In this study we compare the parallax and luminosity distances of a pristine sample of 33 well-known early-type stars with non-peculiar reddening curves and find that the luminosity distance overestimates the parallactic distance in 80% of the cases. This discrepancy can be removed when incorporating a population of large, submicrometer-sized dust grains in a dust model that provides gray extinction which diminishes the luminosity distance accordingly.

Keywords: ISM: clouds – Stars: early-type – (ISM) dust, extinction

1. INTRODUCTION

The distance D of astronomical objects is a fundamental quantity, prompting the exploration of various estimation techniques. The parallax π , based on geometric principles, provides the most straightforward approach but is limited to nearby stars. The luminosity distance D_L enables the assessment of distances of many kpc by measuring the apparent stellar brightness and comparing it with the absolute brightness. However, the apparent brightness of stars is usually diminished by an unknown amount of dust.

Traditionally, the extinction is determined from the apparent color of stars in the visible range (e.g. $B - V$), comparing it with the unreddened color $(B - V)_0$, and multiplying the difference $E(B - V)$ with the ratio of total-to-selective extinction, R_V . The average value of R_V in the Milky Way is ~ 3.1 (Gordon et al. 2023),

with extreme values from 2.1 in clouds of high galactic latitude to 5.6 in dense molecular clouds. It should be noted that R_V corresponds to the extinction at infinite wavelengths and is extrapolated from measurements at near-infrared (NIR) wavelengths. The reddening longward of $2.2\mu\text{m}$ is more difficult to establish because contamination by either dust or any other emission components of early-type stars might play an important role (Siebenmorgen et al. 2018; Deng et al. 2022).

By introducing the photometric equation nearly 100 years ago it was speculated that an additional non-selective or gray extinction term in the form of very large grains – at that time called ‘meteoritic’ bodies – might exist, which increases the extinction term in Eq. 1 by a constant offset but which was arbitrarily set to zero (Trumpler 1930)

$$A_V = V - M_V - 5 \log D_L + 5 . \quad (1)$$

where M_V is the absolute magnitude of the star. Meanwhile, submicrometer-sized particles have been found in various environments (Sect. 4) providing significant wavelength-independent extinction from the far-UV to the NIR. As a consequence, A_V determinations from optical reddening must underestimate the total extinction and thus lead to larger distances. For a few stars, it was hypothesized (Krelowski et al. 2015) that incorporating an additional component of large dust grains could reconcile the problem of missing extinction and thus inaccurate distance estimates; however, this remained unverified due to the lack of a physical model.

In the following we use distances D_{Gaia} , obtained from the zero-point corrected parallax following Lindegren et al. (2021) and compare them with the luminosity distances D_L for a pristine sample of 33 well-known OB stars. For many stars, our investigation uncovers an inconsistency between both methods; its detection required the unprecedented resolution of the Gaia data release three (Gaia Collaboration et al. 2020). To reconcile the discrepancy in distance, we consider a contribution of gray extinction (Eq. 1) due to submicrometer-sized grains. In the ISM a gray component of micrometer-sized grains was introduced by Mathis et al. (1977) and recently by Wang et al. (2015a,b) to account for the observed infrared extinction. Finally, we calibrate the contribution of submicrometer-sized grains to the total extinction with the distance suggested by Gaia.

2. THE SAMPLE

The inclusion of an additional extinction term necessitates validation through a dust model. For such a test a well-selected sample of reddening curves is crucial. The stars shall have precise photometric measurements, accurate distance determinations, rigorous spectral type classifications and luminosity class identifications, allowing reasonable estimates of the absolute brightness M_V , as well as high-quality reddening curves spanning the entire range from the Lyman limit to infinitely long wavelengths.

In that wavelength range, 820 reddening curves have been published by Valencic et al. (2004); Fitzpatrick & Massa (2007); Gordon et al. (2009), which suffer from various systematic uncertainties. To obtain a high-quality sample, Siebenmorgen et al. (2023) inspected and merged a sample of 186 stars, mainly observed with the Ultraviolet and Visual Echelle Spectrograph (UVES; (Dekker et al. 2000)). From this sample, stars with composite spectra in the IUE/FUSE apertures arising from multiple bright stellar systems were excluded. Likewise, stars were omitted with a photometric variability between space (Kharchenko & Roeser 2009; Gaia Collabo-

ration et al. 2018a, 2020) and ground-based observations (Valencic et al. 2004) of more than $\sigma(V) = 30$ mmag, $\sigma(B - V) = 30$ mmag, and $\sigma(G) = 11$ mmag, respectively. Further, stars that show inconsistent parallaxes when comparing data releases two and three from Gaia (Gaia Collaboration et al. 2018a, 2020) were rejected.

The spectral type and luminosity class (SpL) estimates of these stars are important for the determination of the reddening curve and when utilizing M_V for distance estimates (Eq. 1). The SpL were identified by fitting the Gray & Corbally (2014) library to UVES spectra with undetected signatures of binarity or circumstellar line profiles. This provided a precision of half a sub-type/class, which matches the accuracy reached by other studies (Kyritsis et al. 2022; Liu et al. 2019). For the O-stars, it was also confirmed that the SpL classification agrees with that provided by the Galactic O-star survey (Sota et al. 2014). Stars whose classification does not confirm the one used in the reddening curve determination were removed.

We apply even stricter criteria to the Gaia data. Only stars with a renormalized unit weight error (RUWE) below 1.1 are included, ensuring that a single-star model accurately fits the astrometric solution (Luri et al. 2018). Additionally, we re-compute the G -magnitude-dependent error in parallax $\sigma(\pi, G)$ (Eq.A1) following Maíz Apellániz (2022), and only consider stars with a parallax precision of $\pi/\sigma(\pi, G) > 10$. The simple inverse of the DR3 catalogue parallax typically agrees with D_{Gaia} within $1.6 \pm 1.8\%$. Since parallactic distances inherently depend on priors, we verified that our distance estimate D_{Gaia} aligns with other probabilistic distance estimates within 1–2% (Bailer-Jones et al. 2021). From the fifty stars that satisfy the criteria for the reddening curve, an additional 17 stars (34%) were rejected for not meeting the stricter Gaia data requirements. Ultimately, using the most robust sample of reddening curves, spectral classification, and parallaxes currently available, we identified a pristine sample of 33 sightlines toward prominent OB stars within a distance of 2.5 kpc.

3. THE DISTANCE DISCREPANCY

The luminosity distance $D_L(A_V^{\text{Ref}})$ was computed using Hipparcos photometry (Kharchenko & Roeser 2009); spectral types and luminosity classes are from UVES (Siebenmorgen et al. 2023). Absolute magnitudes M_V were calculated from our SpL and the conversion tables (Bowen et al. 2008; Wegner 2006). The visual extinction A_V^{Ref} was obtained by extrapolation of the reddening curves (Valencic et al. 2004; Fitzpatrick & Massa 2007; Gordon et al. 2009). The errors in $D_L(A_V^{\text{Ref}})$ primarily arise from systematic uncertainties. We apply

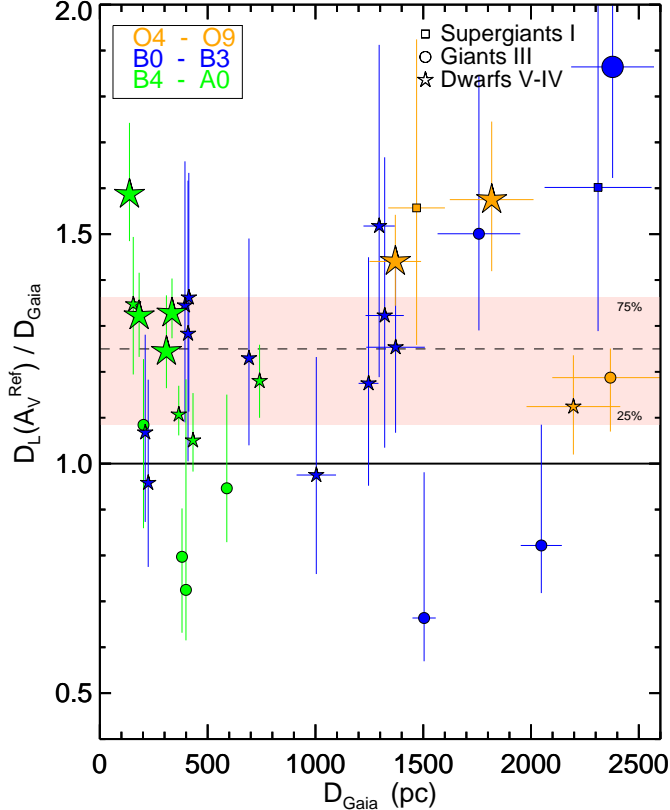


Figure 1. The distance ratios $D_L(A_V^{\text{Ref}})/D_{\text{Gaia}}$ vs. D_{Gaia} for our sample of 33 stars using visual extinction A_V^{Ref} estimates obtained by extrapolation of the reddening curves (Valencic et al. 2004; Fitzpatrick & Massa 2007; Gordon et al. 2009). Different symbols and colors are used to visually represent the various spectral types and luminosity classes as labelled. Stars with a deviation in the distance ratio from unity that are below 3σ in M_V are shown by small symbols. The shaded area depicts the top and bottom quartiles of the distribution, with the mean indicated by a dashed line.

the conservative error estimate $\sigma(M_V)$ in M_V following Bowen et al. (2008). The 1σ scatter between M_V of the spectral type and the adjacent ± 0.5 subtype is denoted as σ_{SpT} , the 1σ scatter between M_V of the luminosity class ± 1 luminosity class is denoted as σ_{LC} . To account for an offset between both catalogues we introduce σ_C ; thus, $\sigma^2(M_V) = \sigma_{\text{SpT}}^2 + \sigma_{\text{LC}}^2 + \sigma_C^2$. For estimating the error in the luminosity distance we add the photometric error $\sigma(V)$. Fig. 1 shows the distance ratios $D_L(A_V^{\text{Ref}})/D_{\text{Gaia}}$ vs. D_{Gaia} for our sample. For the same star, the luminosity distance $D_L(A_V^{\text{Ref}})$ generally overpredicts the Gaia distance D_{Gaia} . There are no stars with a distance ratio below $D_L(A_V^{\text{Ref}})/D_{\text{Gaia}} < 1.25$ de-

tected at 3σ confidence. The distance ratios range between $0.7 \lesssim D_L(A_V^{\text{Ref}})/D_{\text{Gaia}} \lesssim 1.9$. The bottom and top quartiles are at 1.09 and 1.37, which underlines the overprediction in $D_L(A_V^{\text{Ref}})$. A dependency of $D_L(A_V^{\text{Ref}})$ on the spectral types and luminosity classes is not observed. We emphasize that stars of identical spectral types show deviations in opposite directions which excludes any systematic offsets in M_V (Table 1). Therefore, we interpret this discrepancy as to arise from an underestimate of A_V^{Ref} . Recent investigations (Shull & Danforth 2019) were still not able to detect any discrepancy within the errors of the Gaia data release two (Gaia Collaboration et al. 2018b); this could only be brought to light utilizing the unprecedented resolution of the Gaia data release three.

4. THE DUST MODEL INCLUDING SUBMICROMETER-SIZED GRAINS

Our study utilizes a dust model¹ by Siebenmorgen (2023) that aligns with current observational constraints of dust in the diffuse ISM of the Milky Way (Hensley & Draine 2021). It accounts for representative solid phase element abundances of the main absorbing dust components and explains accurately phenomena such as wavelength-dependent reddening, extinction, starlight polarization, and the emission of unpolarized and polarized light seen by Planck (Planck Collaboration et al. 2020). Recently, the (sub)millimeter excess emission in the Milky Way has gained an alternative explanation by adjusting the grain emissivity at these wavelengths (Hensley & Draine 2021) to avoid micrometer-sized cold dust particles. However, these models fail short resolving the distance discrepancy reported in Sect. 3.

The dust model incorporates three populations: 1) nanoparticles of graphite, silicate, and polycyclic aromatic hydrocarbon (PAH), 2) spheroidal grains of amorphous carbon and silicate at mean radii of ~ 30 nm, using the latest optical constants for amorphous silicates (Demyk et al. 2022), and 3) submicrometer-sized dust particles.

Flat infrared extinction curves can also be explained by very porous, fluffy particles (Krügel & Siebenmorgen 1994) with the degree of porosity constrained through a comparison of optical and submillimeter polarization (Guillet et al. 2018). Submicrometer sized grains have been studied by Mathis et al. (1977); Voshchinnikov (2004); Krügel (2008) and have been included in other dust models by Ormel et al. (2011); Ysard et al. (2024). Recently, the impact of gray extinction on type Ia su-

¹ Custom software AbsreDgaia available at https://github.com/rsiebenm/dark_dust

Table 1. Data supporting Fig. 1 and Fig. 2.

1	2	3	4	5	6	7	8	9	10	11
Star	Ref	SpL	M_V (mag)	V (mag)	$E(B - V)$ (mag)	A_V^{Ref} (mag)	A_V (mag)	$D_L(A_V^{\text{Ref}})$ (pc)	D_{Gaia} (pc)	$D_L(A_V)$ (pc)
HD 027778	G	B3V	$-1.52^{+0.39}_{-0.44}$	6.33	0.39	1.09	1.23 ± 0.42	225^{+45}_{-41}	210 ± 3	210
HD 037903	G	B2V	$-2.28^{+0.46}_{-0.46}$	7.84	0.36	1.49	2.13 ± 0.46	531^{+124}_{-100}	395 ± 10	395
HD 038023	F	B3V	$-1.52^{+0.39}_{-0.44}$	8.87	0.52	1.64	2.31 ± 0.42	562^{+112}_{-103}	413 ± 7	413
HD 046223	V	O4V	$-5.65^{+0.13}_{-0.13}$	7.31	0.54	1.48	2.27 ± 0.23	1974^{+126}_{-118}	1371 ± 120	1370
HD 054439	F	B1V	$-3.04^{+0.50}_{-0.53}$	7.71	0.31	0.80	0.75 ± 0.55	979^{+254}_{-212}	1004 ± 92	1004
HD 062542	G	B5V	$-1.21^{+0.12}_{-0.09}$	7.99	0.37	1.16	1.38 ± 0.11	405^{+23}_{-16}	366 ± 5	366
HD 070614	F	B3III	$-2.85^{+0.85}_{-0.33}$	9.29	0.68	2.14	1.93 ± 0.59	998^{+477}_{-139}	1504 ± 54	1101
HD 091824	F	O7V	$-4.90^{+0.21}_{-0.21}$	8.15	0.25	0.77	1.76 ± 0.32	2863^{+293}_{-266}	1817 ± 194	1817
HD 092044	F	B1Ib	$-5.95^{+0.59}_{-0.46}$	8.31	0.43	1.42	2.44 ± 0.58	3702^{+1153}_{-713}	2311 ± 248	2311
HD 093222	G	O6III	$-5.90^{+0.05}_{-0.20}$	8.10	0.36	1.76	2.13 ± 0.28	2812^{+66}_{-243}	2368 ± 270	2368
HD 101008	F	B0III	$-5.00^{+0.42}_{-0.30}$	9.16	0.27	0.93	2.28 ± 0.40	4434^{+951}_{-567}	2378 ± 192	2378
HD 108927	F	B5V	$-1.21^{+0.12}_{-0.09}$	7.77	0.24	0.74	1.36 ± 0.12	444^{+25}_{-18}	335 ± 7	334
HD 110336	F	B8V	$-0.49^{+0.20}_{-0.14}$	8.64	0.45	1.21	1.69 ± 0.18	384^{+38}_{-25}	309 ± 3	309
HD 110946	F	B2III	$-3.55^{+0.60}_{-0.29}$	9.18	0.50	1.60	1.46 ± 0.46	1683^{+537}_{-207}	2048 ± 95	1798
HD 112607	F	B5III	$-1.48^{+0.42}_{-0.29}$	8.10	0.31	0.85	0.77 ± 0.36	557^{+120}_{-69}	589 ± 15	577
HD 112954	F	B9III	$-0.77^{+0.27}_{-0.50}$	8.39	0.57	1.75	1.61 ± 0.39	304^{+40}_{-63}	381 ± 5	324
HD 129557	V	B1V	$-3.04^{+0.50}_{-0.53}$	6.09	0.23	0.53	1.07 ± 0.52	525^{+136}_{-113}	409 ± 17	409
HD 146284	F	B9III	$-0.77^{+0.27}_{-0.50}$	6.71	0.25	0.77	0.95 ± 0.39	219^{+29}_{-45}	202 ± 3	202
HD 146285	F	B9IV	$+0.10^{+0.22}_{-0.26}$	7.93	0.32	1.23	1.88 ± 0.25	209^{+23}_{-24}	155 ± 2	155
HD 147196	F	B8V	$-0.49^{+0.20}_{-0.14}$	7.04	0.27	0.84	1.84 ± 0.18	218^{+21}_{-14}	137 ± 1	137
HD 148594	F	B7V	$-0.67^{+0.15}_{-0.15}$	6.89	0.21	0.65	1.26 ± 0.16	241^{+17}_{-16}	182 ± 2	182
HD 152245	V	B0.5III	$-4.80^{+0.45}_{-0.32}$	8.39	0.36	1.08	1.96 ± 0.45	2639^{+600}_{-358}	1758 ± 192	1758
HD 152249	G	O9Ia	$-7.00^{+0.46}_{-0.46}$	6.38	0.47	1.58	2.54 ± 0.50	2288^{+535}_{-434}	1469 ± 131	1469
HD 170634	F	B8V	$-0.49^{+0.20}_{-0.14}$	9.85	0.69	2.05	2.16 ± 0.18	454^{+45}_{-29}	432 ± 6	432
HD 170740	F	B2V	$-2.28^{+0.46}_{-0.46}$	5.75	0.47	1.37	1.28 ± 0.47	215^{+50}_{-41}	224 ± 12	224
HD 185418	G	B0.5V	$-3.55^{+0.42}_{-0.36}$	7.49	0.52	1.39	1.84 ± 0.40	850^{+180}_{-131}	692 ± 24	692
HD 287150	F	A1III	$+0.73^{+1.06}_{-0.36}$	9.26	0.37	1.22	1.11 ± 0.71	289^{+183}_{-44}	399 ± 5	304
HD 294304	F	B6V	$-0.89^{+0.14}_{-0.15}$	10.05	0.42	1.23	1.59 ± 0.16	874^{+58}_{-59}	741 ± 18	741
HD 303308	V	O6V	$-5.20^{+0.19}_{-0.19}$	8.12	0.45	1.36	1.61 ± 0.29	2469^{+220}_{-202}	2196 ± 217	2196
HD 315021	F	B0V	$-3.85^{+0.34}_{-0.34}$	8.57	0.34	1.24	1.73 ± 0.40	1719^{+287}_{-246}	1372 ± 136	1372
HD 315023	F	B2V	$-2.28^{+0.46}_{-0.46}$	10.03	0.36	1.48	1.83 ± 0.46	1464^{+342}_{-277}	1246 ± 46	1246
HD 315024	F	B1V	$-3.04^{+0.50}_{-0.53}$	9.63	0.30	1.20	2.11 ± 0.53	1966^{+510}_{-425}	1295 ± 73	1295
HD 315032	F	B1V	$-3.04^{+0.50}_{-0.53}$	9.18	0.28	1.01	1.62 ± 0.54	1747^{+453}_{-378}	1321 ± 89	1321

Notes: Reddening curves (column 2) by F (Fitzpatrick & Massa 2007), G (Gordon et al. 2009), V (Valencic et al. 2004); SpL (column 3) by Siebenmorgen et al. (2023) with associated M_V (column 4) by Bowen et al. (2008); Wegner (2006); V -band (column 5) by Kharchenko & Roeser (2009); luminosity distance $D_L(A_V^{\text{Ref}})$ (column 9) using extrapolated A_V^{Ref} (column 7) estimated by the same authors of the reddening curves; luminosity distance $D_L(A_V)$ (column 11) utilizing our estimate of A_V (column 8).

perovae distance measurements has been discussed by the Dark Energy Survey Collaboration (Popovic et al. 2024). Furthermore, micrometer-sized particles from the diffuse ISM were also measured in situ from the Ulysses, Galileo, and Stardust space probes (Landgraf et al. 2000; Westphal et al. 2014; Krüger et al. 2015). They appear in sightlines connected to the cold ISM (Siebenmorgen et al. 2020).

Submicrometer-sized grains absorb a fraction of the interstellar radiation field, ISRF (Mathis et al. 1983). Because these grains are large, they are cold and emit at long wavelengths. Originally very cold (10 K) dust emission was detected in our Galaxy towards high-density regions (Chini et al. 1993) and in non-active galaxies (Chini et al. 1995). Such cold dust was confirmed by ISO (Krügel et al. 1998; Siebenmorgen et al. 1999). More recently, excess emission at 0.5 mm observed by Herschel cannot be explained by a single modified black-body temperature component (Madden et al. 2013; Kennicutt et al. 2011; Rémy-Ruyer et al. 2013); these results were confirmed with ALMA (Galliano et al. 2005) and LABOCA (Galametz et al. 2009) at even longer wavelengths.

5. THE DISTANCE INCLUDING SUBMICROMETER-SIZED GRAINS

Correcting the distance discrepancy is not feasible through arbitrary adjustments to commonly used literature values in $A_V^{\text{Ref}} = R_V/E(B-V)$ and M_V inserted in Eq. 1. Several stars with identical SpL show different distance ratios and thus would require different adjustments in M_V to reach $D_L = D_{\text{Gaia}}$. The uncertainties in M_V range from 0.25 to 0.5 mag. However, for stars with $D_L/D_{\text{Gaia}} \gtrsim 1.2$, modifications of $M_V > 0.5$ mag, – typically 0.8 ± 0.3 mag – would be necessary to align D_L with D_{Gaia} . Similarly, the typical error in $E(B-V)$ is around 0.03 mag; for stars with $D_L/D_{\text{Gaia}} \gtrsim 1.2$, modifications of $0.14 \lesssim E(B-V) \lesssim 0.56$ mag would be required to achieve distance unification. Consequently, we retain $E(B-V)$ and substitute the extrapolated R_V parameter with our dust model, utilizing Eqs. A2 - A3.

Fig. 2 shows the corrected distance ratios $D_L(A_V)/D_{\text{Gaia}}$ vs. D_{Gaia} for our sample, where $D_L(A_V)$ denotes the luminosity distance derived from A_V using Eq. 1. The new luminosity distances $D_L(A_V)$, agree with D_{Gaia} within $0.75 < D_L(A_V)/D_{\text{Gaia}} \lesssim 1$ and show a 1σ scatter of 6% around a median of one. The four stars with $D_L(A_V) > D_{\text{Gaia}}$ still agree within their errors with equal distances $D_L(A_V) = D_{\text{Gaia}}$. For 29 out of 33 stars both distances agree within 2%. Their scatter of the distance ratio is reduced by a factor of

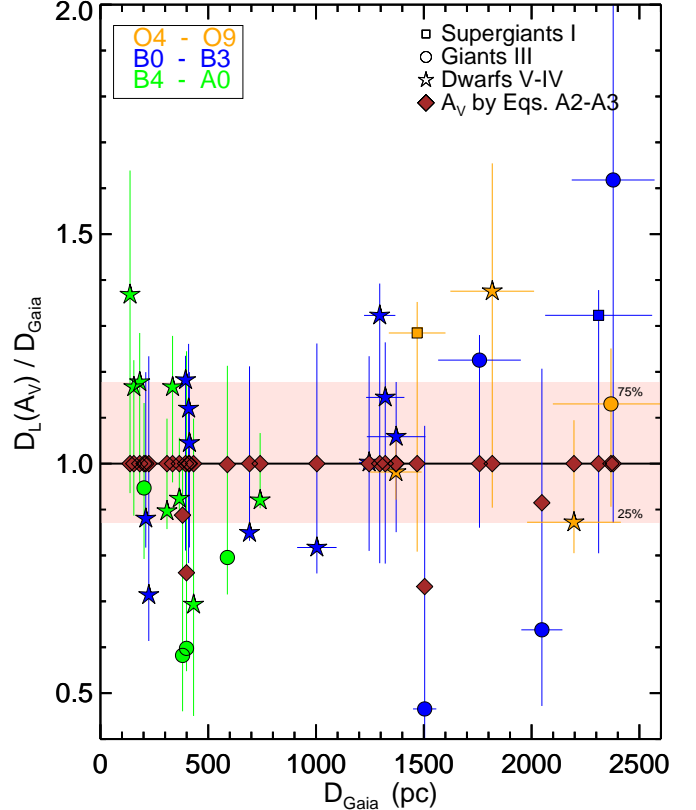


Figure 2. Corrected distance ratios $D_L(A_V)/D_{\text{Gaia}}$ vs. D_{Gaia} . The luminosity distance derived with A_V using Eqs. A2-A3 (diamonds in brown) unifies the distance ratio for all but four stars. These four stars still agree within their errors with a ratio of one. For comparison, the luminosity distance determined from A_V is derived by a single-parameter model fit to the reddening in the $UBVJHK$ bands, assuming a mass fraction of submicrometer particles of 0.55 g in a total of 1 g of dust (symbols in color, as denoted in Fig. 1). The shaded area depicts the top and bottom quartiles of the single-parameter model distribution, with a mean of one (solid line).

five when compared to the literature values $D_L(A_V^{\text{Ref}})$, which are, for ease of comparison, also shown in Fig. 2.

The reliability of the A_V estimate (Eq. 1) is validated through fitting the absolute reddening curve across the entire observed wavelength range using the three-component dust model, which incorporates submicrometer-sized grains. Models that incorporate a simple continuation of the dust size distribution to micrometers for the amorphous carbon and silicate grains or ignore submicrometer-sized grains fail to align to ex-

plain the reddening at $\lambda > 1\mu\text{m}$ and often violate abundance constraints (Table 3).

The submicrometer-sized dust population typically contributes to one-third of the total extinction A_V . This dust component constitutes $56 \pm 12\%$ of the total dust mass and depends on the environmental conditions and chemical composition of the clouds along the sightlines. Note that the total gas-to-dust mass ratio remains unchanged in the models $M_{\text{gas}}/M_{\text{dust}}$ (Table 2). The addition of submicrometer-sized grains only affects the relative mass distribution of different dust particle types within 1 g of dust (Eq. B4). It does not change the total dust mass or the amount of elements depleted from the gas phase (Table 3). Models that ignore the submicrometer-sized grain component or merely extend the size distribution of amorphous particle components from 250 nm to a few microns often fail to explain the reddening at $\lambda > 1\mu\text{m}$ and violate abundance constraints. This is evident when comparing the goodness-of-fit to the IR data for models with, χ_{IR}^2 , and without, $\chi_{\text{IR}}^{2,\text{no-}s\mu}$, submicrometer-sized grains, as $\chi_{\text{IR}}^2 < \chi_{\text{IR}}^{2,\text{no-}s\mu}$ (Table 3).

Without knowledge of the trigonometric distance, one can assume that half of the dust mass resides in submicrometer grains to account for the offset in the luminosity distance reported in Fig. 1. This is demonstrated in Fig. 2 using a single-parameter model² to fit the reddening in the *UBVJHK* bands. The visual extinction A_V is derived from the reddening at infinite wavelengths based on the best-fit model, with the carbon abundance in amorphous grains treated as the only free parameter.

6. CONCLUSION

We derived the visual extinction through the diffuse ISM from a comparison of the luminosity distance and the trigonometric distance of 33 nearby ($\lesssim 2.5$ kpc) early-type stars using the most comprehensive sample of reddening curves and SpL identifications currently accessible. Our analysis supports the presence of a submicrometer-sized dust population in 80% of the sightlines, consistent with the dust model introduced by Mathis et al. (1977) and employed to explain IR reddening by Wang et al. (2015a). Due to the wavelength-independent extinction of such very large grains such a population is hidden in photometric data from the optical/far UV range. Dust models ignoring the submicrometer-sized grain component thus underestimate the total extinction of the sightline and – as a

consequence – resulting in significantly larger distance estimates when applying traditional photometric distance measurements.

Apart from the importance of the gray extinction component, our study has developed a consistent dust model that satisfies contemporary constraints on dust in the general ISM field (Hensley & Draine 2021) and aligns with the available data for individual sightlines in our sample. We also provide a single-parameter model to fit the optical/IR reddening and correct the average overprediction in the luminosity distance for the sample, even when assuming the parallax is unknown.

The dust model respects estimates of the visual extinction derived from the Gaia parallax. Our study emphasizes the significance of considering the absolute reddening of individual sightlines across the entire wavelength range and in particular in the IR instead of utilizing the extrapolated parameter R_V .

Besides our own ongoing efforts to increase the sample size and enhance statistical robustness, we hope to inspire the community to further test the model using the custom software provided. To better constrain the population of submicrometer-sized grains in the diffuse ISM, targeted observations should focus on stars with known spectral types, luminosity classes, and precise trigonometric distances provided by Gaia or VLTI. For these stars, the depletion of elements such as C, Si, Mg, Fe, O, and Al from the gas phase should be measured. These elements contribute significantly to the dust extinction. For these sightlines, the reddening $E(\lambda - V)$ should be well established in the far UV, around the 2175 Å bump, and in the NIR/MIR. The latter can be complemented by observations with the JWST, which offers spectral information that can potentially detect or provide stringent upper limits on ice absorption bands in the diffuse ISM. The silicate stoichiometry can be revealed through MIR spectro-polarimetry (Wright et al. 2002). The geometry and particle shape of submicrometer-sized grains can be determined by combining high spatial resolution observations of polarized emission in the millimeter continuum, as provided by BLAST (Coppi et al. 2024), with dichroic polarization of starlight in the optical (Bagnulo et al. 2017). Such studies of submicrometer-sized grains appear also of interest for dark energy surveys, as analyzed by Popovic et al. (2024).

We are grateful to Tereza Jerabkova and Miguel Vioque for discussions of Gaia distances.

² Custom software `1_absReddEbv` available at https://github.com/rsiebenm/dark_dust

REFERENCES

- Bagnulo, S., Cox, N. L. J., Cikota, A., et al. 2017, *A&A*, 608, A146, doi: [10.1051/0004-6361/201731459](https://doi.org/10.1051/0004-6361/201731459)
- Bailer-Jones, C. A. L., Rybizki, J., Fouesneau, M., Demleitner, M., & Andrae, R. 2021, *AJ*, 161, 147, doi: [10.3847/1538-3881/abd806](https://doi.org/10.3847/1538-3881/abd806)
- Bowen, D. V., Jenkins, E. B., Tripp, T. M., et al. 2008, *ApJS*, 176, 59, doi: [10.1086/524773](https://doi.org/10.1086/524773)
- Chini, R., Krügel, E., Haslam, C. G. T., et al. 1993, *A&A*, 272, L5
- Chini, R., Krügel, E., Lemke, R., & Ward-Thompson, D. 1995, *A&A*, 295, 317
- Coppi, G., Dicker, S., Aguirre, J. E., et al. 2024, *Publications of the Astronomical Society of the Pacific*, 136, 035003, doi: [10.1088/1538-3873/ad2e11](https://doi.org/10.1088/1538-3873/ad2e11)
- Dekker, H., D’Odorico, S., Kaufer, A., Delabre, B., & Kotzlowski, H. 2000, in *Society of Photo-Optical Instrumentation Engineers (SPIE) Conference Series*, Vol. 4008, *Optical and IR Telescope Instrumentation and Detectors*, ed. M. Iye & A. F. Moorwood, 534–545, doi: [10.1117/12.395512](https://doi.org/10.1117/12.395512)
- Demyk, K., Gromov, V., Meny, C., et al. 2022, *arXiv e-prints*, arXiv:2209.06513. <https://arxiv.org/abs/2209.06513>
- Deng, D., Sun, Y., Wang, T., Wang, Y., & Jiang, B. 2022, *ApJ*, 935, 175, doi: [10.3847/1538-4357/ac8168](https://doi.org/10.3847/1538-4357/ac8168)
- Draine, B. T. 2003, *ARA&A*, 41, 241, doi: [10.1146/annurev.astro.41.011802.094840](https://doi.org/10.1146/annurev.astro.41.011802.094840)
- Draine, B. T., & Hensley, B. S. 2021, *ApJ*, 909, 94, doi: [10.3847/1538-4357/abd6c6](https://doi.org/10.3847/1538-4357/abd6c6)
- Fitzpatrick, E. L., & Massa, D. 2007, *ApJ*, 663, 320, doi: [10.1086/518158](https://doi.org/10.1086/518158)
- Gaia Collaboration, Brown, A. G. A., Vallenari, A., et al. 2020, *arXiv e-prints*, arXiv:2012.01533. <https://arxiv.org/abs/2012.01533>
- . 2018a, *A&A*, 616, A1, doi: [10.1051/0004-6361/201833051](https://doi.org/10.1051/0004-6361/201833051)
- . 2018b, *A&A*, 616, A1, doi: [10.1051/0004-6361/201833051](https://doi.org/10.1051/0004-6361/201833051)
- Galametz, M., Madden, S., Galliano, F., et al. 2009, *A&A*, 508, 645, doi: [10.1051/0004-6361/200912963](https://doi.org/10.1051/0004-6361/200912963)
- Galliano, F., Madden, S. C., Jones, A. P., Wilson, C. D., & Bernard, J. P. 2005, *A&A*, 434, 867, doi: [10.1051/0004-6361:20042369](https://doi.org/10.1051/0004-6361:20042369)
- Gordon, K. D., Cartledge, S., & Clayton, G. C. 2009, *ApJ*, 705, 1320, doi: [10.1088/0004-637X/705/2/1320](https://doi.org/10.1088/0004-637X/705/2/1320)
- Gordon, K. D., Clayton, G. C., Declair, M., et al. 2023, *ApJ*, 950, 86, doi: [10.3847/1538-4357/accb59](https://doi.org/10.3847/1538-4357/accb59)
- Gray, R. O., & Corbally, C. J. 2014, *AJ*, 147, 80, doi: [10.1088/0004-6256/147/4/80](https://doi.org/10.1088/0004-6256/147/4/80)
- Guillet, V., Fanciullo, L., Verstraete, L., et al. 2018, *A&A*, 610, A16, doi: [10.1051/0004-6361/201630271](https://doi.org/10.1051/0004-6361/201630271)
- Hensley, B. S., & Draine, B. T. 2021, *ApJ*, 906, 73, doi: [10.3847/1538-4357/abc8f1](https://doi.org/10.3847/1538-4357/abc8f1)
- Kennicutt, R. C., Calzetti, D., Aniano, G., et al. 2011, *PASP*, 123, 1347, doi: [10.1086/663818](https://doi.org/10.1086/663818)
- Kharchenko, N. V., & Roeser, S. 2009, *VizieR Online Data Catalog*, I/280B
- Krelowski, J., Galazutdinov, G. A., Mulas, G., Maszewska, M., & Cecchi-Pestellini, C. 2015, *MNRAS*, 451, 3210, doi: [10.1093/mnras/stv1117](https://doi.org/10.1093/mnras/stv1117)
- Krügel, E. 2008, *An introduction to the physics of interstellar dust (IOP)*, doi: [10.1063/1.3001869](https://doi.org/10.1063/1.3001869)
- Krügel, E., & Siebenmorgen, R. 1994, *A&A*, 288, 929
- Krügel, E., Siebenmorgen, R., Zota, V., & Chini, R. 1998, *A&A*, 331, L9
- Krüger, H., Strub, P., Grün, E., & Sterken, V. J. 2015, *ApJ*, 812, 139, doi: [10.1088/0004-637X/812/2/139](https://doi.org/10.1088/0004-637X/812/2/139)
- Kyritsis, E., Maravelias, G., Zezas, A., et al. 2022, *A&A*, 657, A62, doi: [10.1051/0004-6361/202040224](https://doi.org/10.1051/0004-6361/202040224)
- Landgraf, M., Baggaley, W. J., Grün, E., Krüger, H., & Linkert, G. 2000, *J. Geophys. Res.*, 105, 10343, doi: [10.1029/1999JA900359](https://doi.org/10.1029/1999JA900359)
- Lindgren, L., Bastian, U., Biermann, M., et al. 2021, *A&A*, 649, A4, doi: [10.1051/0004-6361/202039653](https://doi.org/10.1051/0004-6361/202039653)
- Liu, Z., Cui, W., Liu, C., et al. 2019, *ApJS*, 241, 32, doi: [10.3847/1538-4365/ab0a0d](https://doi.org/10.3847/1538-4365/ab0a0d)
- Luri, X., Brown, A. G. A., Sarro, L. M., et al. 2018, *A&A*, 616, A9, doi: [10.1051/0004-6361/201832964](https://doi.org/10.1051/0004-6361/201832964)
- Madden, S. C., Rémy-Ruyer, A., Galametz, M., et al. 2013, *PASP*, 125, 600, doi: [10.1086/671138](https://doi.org/10.1086/671138)
- Maíz Apellániz, J. 2022, *A&A*, 657, A130, doi: [10.1051/0004-6361/202142365](https://doi.org/10.1051/0004-6361/202142365)
- Markwardt, C. B. 2009, in *Astronomical Society of the Pacific Conference Series*, Vol. 411, *Astronomical Data Analysis Software and Systems XVIII*, ed. D. A. Bohlender, D. Durand, & P. Dowler, 251. <https://arxiv.org/abs/0902.2850>
- Mathis, J. S., Mezger, P. G., & Panagia, N. 1983, *A&A*, 128, 212
- Mathis, J. S., Ruml, W., & Nordsieck, K. H. 1977, *ApJ*, 217, 425, doi: [10.1086/155591](https://doi.org/10.1086/155591)
- Ormel, C. W., Min, M., Tielens, A. G. G. M., Dominik, C., & Paszun, D. 2011, *A&A*, 532, A43, doi: [10.1051/0004-6361/201117058](https://doi.org/10.1051/0004-6361/201117058)
- Planck Collaboration, Aghanim, N., Akrami, Y., et al. 2020, *A&A*, 641, A12, doi: [10.1051/0004-6361/201833885](https://doi.org/10.1051/0004-6361/201833885)

- Popovic, B., Wiseman, P., Sullivan, M., et al. 2024, Modelling the impact of host galaxy dust on type Ia supernova distance measurements. <https://arxiv.org/abs/2406.05051>
- Rémy-Ruyer, A., Madden, S. C., Galliano, F., et al. 2013, *A&A*, 557, A95, doi: [10.1051/0004-6361/201321602](https://doi.org/10.1051/0004-6361/201321602)
- Shull, J. M., & Danforth, C. W. 2019, *ApJ*, 882, 180, doi: [10.3847/1538-4357/ab357d](https://doi.org/10.3847/1538-4357/ab357d)
- Siebenmorgen, R. 2023, *A&A*, 670, A115, doi: [10.1051/0004-6361/202243860](https://doi.org/10.1051/0004-6361/202243860)
- Siebenmorgen, R., Krelowski, J., Smoker, J., Galazutdinov, G., & Bagnulo, S. 2020, *A&A*, 641, A35, doi: [10.1051/0004-6361/202037511](https://doi.org/10.1051/0004-6361/202037511)
- Siebenmorgen, R., Krügel, E., & Chini, R. 1999, *A&A*, 351, 495
- Siebenmorgen, R., Scicluna, P., & Krelowski, J. 2018, *A&A*, 620, A32, doi: [10.1051/0004-6361/201833546](https://doi.org/10.1051/0004-6361/201833546)
- Siebenmorgen, R., Smoker, J., Krelowski, J., Gordon, K., & Chini, R. 2023, *A&A*, 676, A132, doi: [10.1051/0004-6361/202244594](https://doi.org/10.1051/0004-6361/202244594)
- Sota, A., Apellániz, J. M., Morrell, N. I., et al. 2014, *A&AS*, 211, 10, doi: [10.1088/0067-0049/211/1/10](https://doi.org/10.1088/0067-0049/211/1/10)
- Trumpler, R. J. 1930, *PASP*, 42, 214, doi: [10.1086/124039](https://doi.org/10.1086/124039)
- Valencic, L. A., Clayton, G. C., & Gordon, K. D. 2004, *ApJ*, 616, 912, doi: [10.1086/424922](https://doi.org/10.1086/424922)
- Voshchinnikov, N. V. 2004, *Astrophys. Space Phys. Res.*, 12, 1
- Voshchinnikov, N. V., & Farafonov, V. G. 1993, *Ap&SS*, 204, 19, doi: [10.1007/BF00658095](https://doi.org/10.1007/BF00658095)
- Wang, S., Li, A., & Jiang, B. W. 2015a, *MNRAS*, 454, 569, doi: [10.1093/mnras/stv1900](https://doi.org/10.1093/mnras/stv1900)
- . 2015b, *ApJ*, 811, 38, doi: [10.1088/0004-637X/811/1/38](https://doi.org/10.1088/0004-637X/811/1/38)
- Wegner, W. 2006, *MNRAS*, 371, 185, doi: [10.1111/j.1365-2966.2006.10549.x](https://doi.org/10.1111/j.1365-2966.2006.10549.x)
- Westphal, A. J., Stroud, R. M., Bechtel, H. A., et al. 2014, *Science*, 345, 786, doi: [10.1126/science.1252496](https://doi.org/10.1126/science.1252496)
- Wright, C. M., Aitken, D. K., Smith, C. H., Roche, P. F., & Laureijs, R. J. 2002, in *The Origin of Stars and Planets: The VLT View*, ed. J. F. Alves & M. J. McCaughrean, 85, doi: [10.1007/10856518_10](https://doi.org/10.1007/10856518_10)
- Ysard, N., Jones, A. P., Guillet, V., et al. 2024, arXiv e-prints, arXiv:2401.07739, doi: [10.48550/arXiv.2401.07739](https://doi.org/10.48550/arXiv.2401.07739)

APPENDIX

A. ABSOLUTE REDDENING

The amount of visual extinction, denoted by A_V , which is necessary to align D_L with D_{Gaia} is calculated using the photometric equation (Eq. 1) with errors including G -band brightness corrections by Maíz Apellániz (2022)

$$\sigma(A_V)^2 = \sigma(V)^2 + \sigma(M_V)^2 + \left(\frac{5}{\log 10} \frac{\sigma(\pi, G)}{D_{\text{Gaia}}} \right)^2 \quad (\text{A1})$$

The optical depth $\tau_V = A_V/1.086$ is related to the column densities of nanoparticles and the amorphous carbon and silicate particles N_n and to the column density of submicrometer-sized grains $N_{s\mu}$; the corresponding mass extinction cross-section K_n and $K_{s\mu}$ (g/cm^3) are based on the dust model (Siebenmorgen 2023):

$$\tau_V = N^n K_V^n + N^{s\mu} K_V^{s\mu} . \quad (\text{A2})$$

The extinction cross-section (Draine 2003; Voshchinnikov 2004; Krügel 2008) diminishes at infinite wavelengths, i.e. $K(\infty) = 0$. To prevent negative optical depths, we assume that the reddening at infinite wavelengths is smaller than in the K -band, hence $A_V = -E(\infty) > -E(K)$, and ignore models not respecting this condition. The reddening $E(B - V) = 1.086 (\tau_B - \tau_V)$ provides a second constraint:

$$\tau_B - \tau_V = N^n (K_B^n - K_V^n) + N^{s\mu} (K_B^{s\mu} - K_V^{s\mu}) . \quad (\text{A3})$$

These two equations enable us to derive the relative mass of each component, specifically $m_n = N_n/(N_n + N_{s\mu})$ of the nano- and amorphous grains and $m_{s\mu} = N_{s\mu}/(N_n + N_{s\mu})$ of the submicrometer-sized particles. Notably, our approach to computing A_V is validated through a fit to the observed reddening curve using our dust model and obviates the need for the extrapolated parameter $R_V = A_V/E(B - V)$.

B. FITTING REDDENING CURVES

The methodology for calculating the wavelength-dependent extinction cross-section $K(\lambda)$ for partially aligned and wobbling spheroidal grains, nanoparticles, and PAH, from the optical constants of dust materials is outlined in Siebenmorgen (2023). The normalized reddening curves $E(\lambda - V)/E(B - V)$ for the sample are observed spectroscopically between $0.09 - 0.27 \mu\text{m}$ with IUE/FUSE satellites and in the UBV - and JHK -bands with references listed in column 2 of Table 1. These curves are transformed into absolute reddening that are used in this work by multiplying them with the corresponding reddening $E(B - V)$ provided in those same references. The extrapolated reddening at infinitely long wavelengths is substituted with the visual extinction A_V , derived from Eq. 1, and are specified in Table 1. By adjusting grain sizes and abundances within the three populations, we achieve the best fit for the absolute reddening curve of each star, surpassing previous models that solely addressed relative reddening or extinction curves.

To achieve the optimal fits for the reddening curves, a set of seven best-fit parameters was computed by a least χ^2 -technique using the Levenberg–Marquardt algorithm as implemented in MPFIT³ (Markwardt 2009). The distribution of the various grain components in 1 g of dust is treated as a set of free parameters, defined by the relative mass of the submicrometer-sized grains ($m_{s\mu}$), the amorphous silicates (m_{Si}) and carbon (m_{aC}), and the nanoparticles of silicates (m_{vSi}), graphite (m_{vgr}), and PAH (m_{PAH}). The relative mass of component i in 1 g of dust, is computed from

$$m_i = \frac{\mu_i \frac{[X_i]}{[H]}}{\sum_i \mu_i \frac{[X_i]}{[H]}} , \quad (\text{B4})$$

where the relative dust abundances of an element, which is in our models either C or Si, with respect to H are denoted by $[X_i]/[H]$ and the molecular weights μ_i as specified in Table 2.

³ <http://purl.com/net/mpfit>

Models that violate the depletion constraints for C and Si atoms, specifically $C/Si < 5.2$ (Hensley & Draine 2021; Siebenmorgen 2023) are excluded. The total dust mass M_{dust} is estimated by summing all atoms depleted from the gas phase and scaling by the molecular weights corresponding to the assumed grain stoichiometry. The gas mass $M_{\text{gas}} \sim 1.4 M_{\text{H}}$ is calculated by summing the contributions of helium and hydrogen, assuming a He:H ratio of 1:10. The derived gas-to-dust mass ratio, $M_{\text{gas}}/M_{\text{dust}} \sim 125$ (Hensley & Draine 2021), remains approximately constant (Table 2). Consequently, the relative mass distribution in 1 g of dust in our models aligns with the material available in the ISM for grain formation.

A power-law dust size distribution is characterized by the exponent q and the lower and upper radii. For amorphous carbon and silicate grains, we use a minimum radius of 6 nm. Following Mathis et al. (1977), we set the relatively unconstrained upper radii to fixed values, with $r_{\text{Si}}^+ = r_{\text{aC}}^+ = 250$ nm, which also serves as the minimum radius for the submicrometer grains, and $r_{\text{s}\mu}^+ = 3\mu\text{m}$. The mass extinction cross sections $K_i(r)$ ($\text{cm}^2/\text{g-dust}$) of a dust particle of population i with volume averaged radius r and bulk density ρ_i is

$$K_i(r) = \frac{m_i}{\frac{4\pi}{3} \rho_i} \frac{r^{-q}}{\int_{r_{-,i}}^{r_{+,i}} r^{3-q} dr} C_i(r). \quad (\text{B5})$$

The cross sections C are derived using efficiency factors Q , and are computed for spheroids using Voshchinnikov & Farafonov (1993) and custom software provided by Voshchinnikov (2004). Fine-tuning of the fits to the 2175 Å bump involves allowing the central wavelength (x_0) and damping constant (γ) of the Lorentzian profiles of PAH absorption cross-section to remain free. This leads to in total seven adjustable parameters which are treated in the minimization algorithm.

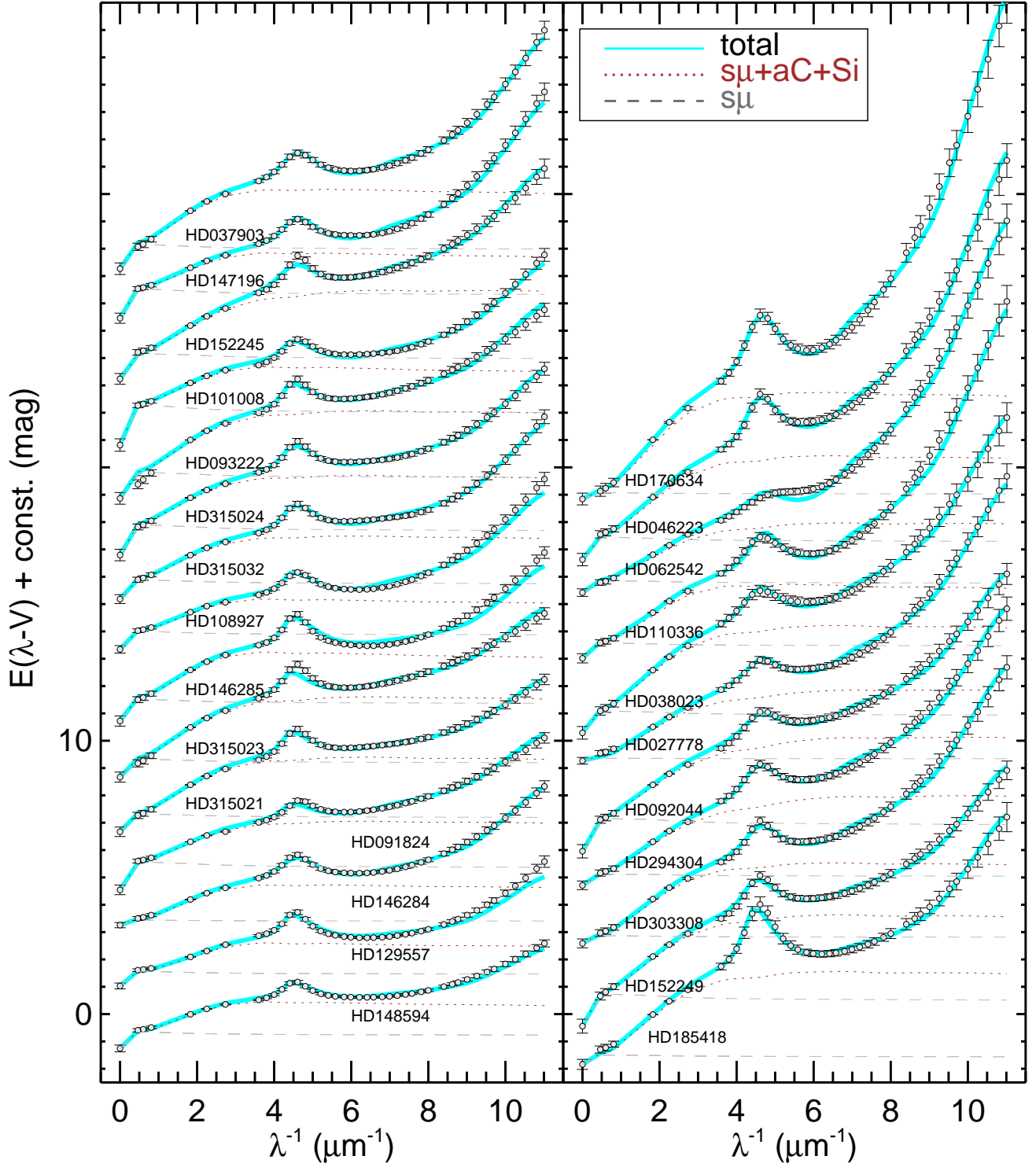


Figure 3. The absolute reddening curves $E(\lambda - V)$ of the sample, shifted by an offset for better visibility. Data points (circles) cover the range $0.09 - 2.2 \mu\text{m}$ and are complemented at infinite wavelengths by $-A_V$ (Table 1). The best fit (cyan) with contributions from the amorphous carbon and silicates (brown), and submicrometer-sized grains (gray), are shown, with model parameters listed in Table 3. Notable is the dominance of the submicrometer-sized grains in the infrared and their wavelength-independent contribution to the optical/far UV, respectively.

Table 2. Dust abundances (ppm), gas-to-dust mass ratios, molecular weights and bulk densities of the best-fit.

Star	$\frac{[C]}{[H]}_{\text{tot}}$	$\frac{[C]}{[H]}_{s\mu}$	$\frac{[C]}{[H]}_{aC}$	$\frac{[C]}{[H]}_{vgr}$	$\frac{[C]}{[H]}_{PAH}$	$\frac{[Si]}{[H]}_{\text{tot}}$	$\frac{[Si]}{[H]}_{s\mu}$	$\frac{[Si]}{[H]}_{aSi}$	$\frac{[Si]}{[H]}_{vSi}$	$\frac{M_{\text{gas}}}{M_{\text{dust}}}$
HD 027778	95	23	48	15	9	37	8	18	11	125
HD 037903	136	48	63	19	6	44	16	20	9	116
HD 038023	91	36	37	12	5	39	12	19	8	125
HD 046223	89	40	25	20	4	44	13	20	11	123
HD 062542	86	41	21	13	11	52	13	20	18	120
HD 091824	89	42	34	9	4	39	14	19	6	125
HD 092044	90	39	36	11	5	39	13	19	7	125
HD 093222	103	37	51	11	4	34	12	17	5	125
HD 101008	103	48	37	13	5	43	16	20	7	121
HD 108927	100	45	32	19	4	43	15	20	8	122
HD 110336	78	39	14	23	2	45	13	20	12	124
HD 129557	76	41	8	19	8	42	13	24	4	126
HD 146284	97	32	40	16	9	37	10	19	7	125
HD 146285	106	37	48	17	5	33	12	18	4	125
HD 147196	108	50	30	21	6	47	16	20	10	119
HD 148594	97	39	40	13	5	36	13	20	4	125
HD 152245	93	38	37	10	8	38	12	19	6	125
HD 152249	94	38	38	10	7	38	12	20	6	125
HD 170634	85	27	31	22	5	41	9	20	12	125
HD 185418	98	29	41	17	11	34	10	20	5	125
HD 294304	92	32	39	14	6	38	10	19	9	125
HD 303308	93	31	42	15	6	38	10	19	9	125
HD 315021	102	36	51	10	5	35	12	19	4	125
HD 315023	103	35	55	7	7	34	11	18	5	125
HD 315024	103	38	47	13	5	34	12	16	5	125
HD 315032	129	45	57	22	5	42	15	20	8	118
μ	12	12	12	12	12		135	100	135	
ρ (g/cm ³)		1.8	1.6	2.2			3.4	2.7	3.5	

Notes: Assumed stoichiometry of silicate material in nano and submicrometer particles is the nominal of $\text{Mg}_{1.3}(\text{Fe,Ni})_{0.3}\text{SiO}_{3.6}$ by Draine & Hensley (2021) and for amorphous silicates the 97:3 mix in mass composed of MgSiO_3 and $\text{Mg}_{0.8}\text{Fe}_{0.2}^{2+}\text{SiO}_3$ by Demyk et al. (2022).

Table 3. Model parameters for fits to the absolute reddening curve.

Star	$m_{s\mu}$ (%)	m_{Si} (%)	m_{vSi} (%)	m_{aC} (%)	m_{vgr} (%)	m_{PAH} (%)	q	χ^2	χ_{IR}^2	$\chi_{IR}^{2,no-s\mu}$
HD 027778	31	30	25	9	3	2	2.7	0.9	2.4	5.8
HD 037903	63	17	10	7	2	1	2.2	0.6	1.3	43.3*
HD 038023	56	23	13	6	2	1	2.5	0.7	0.1	39.9
HD 046223	55	22	16	3	3	1	2.4	1.0	0.5	60.0
HD 062542	46	22	26	3	2	1	2.5	1.4	0.7	10.7
HD 091824	69	18	8	4	1	0	2.4	0.6	0.4	151.8*
HD 092044	62	21	10	5	1	1	2.7	0.6	0.1	92.4*
HD 093222	64	20	8	7	1	1	2.4	1.4	11.6	16.6*
HD 101008	74	14	7	3	1	0	2.1	0.9	0.2	251.8*
HD 108927	66	18	10	3	2	0	2.0	1.5	0.1	62.4*
HD 110336	53	23	18	2	3	0	2.2	1.3	0.1	21.6
HD 129557	66	24	6	1	2	1	2.0	1.7	0.3	61.2*
HD 146284	48	27	14	7	3	2	2.1	0.4	0.2	5.9*
HD 146285	66	19	5	6	2	1	2.0	2.0	0.4	52.2*
HD 147196	69	15	11	3	2	1	2.1	0.9	0.1	142.5*
HD 148594	68	19	5	5	2	1	2.0	0.6	0.3	70.1*
HD 152245	62	22	9	5	1	1	2.6	0.7	0.6	85.8*
HD 152249	63	22	8	5	1	1	2.5	0.6	0.2	87.8*
HD 170634	36	30	24	6	4	1	2.3	1.3	0.1	2.5
HD 185418	47	31	9	7	3	2	2.5	0.9	2.1	18.6
HD 294304	47	27	16	7	2	1	2.7	0.6	0.1	11.7
HD 303308	44	27	17	7	3	1	2.5	0.7	0.3	7.6
HD 315021	61	23	6	7	1	1	2.4	0.4	0.5	28.2*
HD 315023	59	23	8	8	1	1	2.4	1.0	2.2	15.8*
HD 315024	68	17	7	6	2	1	2.4	0.4	0.7	95.3*
HD 315032	63	18	9	6	2	0	2.3	0.4	0.1	49.7*

Notes: The symbol * indicates that abundance constraints are violated.